

Static-to-kinematic modeling and experimental validation of tendon-driven quasi continuum manipulators with nonconstant subsegment stiffness

Xian-Jie Zheng(郑先杰), Meng Ding(丁萌), Liao-Xue Liu(刘辽雪), Lu Wang(王璐), and Yu Guo(郭毓)
Citation: Chin. Phys. B, 2024, 33 (**1**): 010703. DOI: 10.1088/1674-1056/acfaf8
Journal homepage: http://cpb.iphy.ac.cn; http://iopscience.iop.org/cpb

What follows is a list of articles you may be interested in

Real-time programmable coding metasurface antenna for multibeam switching and scanning

Jia-Yu Yu(余佳宇), Qiu-Rong Zheng(郑秋容)†, Bin Zhang(张斌), Jie He(贺杰), Xiang-Ming Hu(胡湘明), and Jie Liu(刘杰)
Chin. Phys. B, 2022, 31 (**9**): 090704. DOI: 10.1088/1674-1056/ac80b2

A comparative study on radiation reliability of composite channel InP high electron mobility transistors

Jia-Jia Zhang(张佳佳), Peng Ding(丁芃), Ya-Nan Jin(靳雅楠), Sheng-Hao Meng(孟圣皓), Xiang-Qian Zhao(赵向前), Yan-Fei Hu(胡彦飞), Ying-Hui Zhong(钟英辉), and Zhi Jin(金智)
Chin. Phys. B, 2021, 30 (**7**): 070702. DOI: 10.1088/1674-1056/abe2fd

Magnetic shielding property for cylinder with circular, square, and equilateral triangle holes

Si-Yuan Hao(郝思源), Xiao-Ping Lou(娄小平), Jing Zhu(祝静), Guang-Wei Chen(陈广伟), and Hui-Yu Li(李慧宇)
Chin. Phys. B, 2021, 30 (**6**): 060702. DOI: 10.1088/1674-1056/abeeee

Efficient sampling for decision making in materials discovery

Yuan Tian(田原), Turab Lookman, and Dezhen Xue(薛德祯)
Chin. Phys. B, 2021, 30 (**5**): 050705. DOI: 10.1088/1674-1056/abf12d

Theoretical analysis and experimental validation of radial cascaded composite ultrasonic transducer

Xiao-Yu Wang(王晓宇), Zhi-Xin Yu(余芷欣), Jing Hu(胡静), and Shu-Yu Lin(林书玉)
Chin. Phys. B, 2021, 30 (**4**): 040701. DOI: 10.1088/1674-1056/abd399

Static-to-kinematic modeling and experimental validation of tendon-driven quasi continuum manipulators with nonconstant subsegment stiffness

Xian-Jie Zheng(郑先杰), Meng Ding(丁萌), Liao-Xue Liu(刘辽雪), Lu Wang(王璐), and Yu Guo(郭毓)†

School of Automation, Nanjing University of Science and Technology, Nanjing 210094, *China*

(Received 18 July 2023; revised manuscript received 22 August 2023; accepted manuscript online 19 September 2023)

Continuum robots with high flexibility and compliance have the capability to operate in confined and cluttered environments. To enhance the load capacity while maintaining robot dexterity, we propose a novel non-constant subsegment stiffness structure for tendon-driven quasi continuum robots (TDQCRs) comprising rigid-flexible coupling subsegments. Aiming at real-time control applications, we present a novel static-to-kinematic modeling approach to gain a comprehensive understanding of the TDQCR model. The analytical subsegment-based kinematics for the multisection manipulator is derived based on screw theory and product of exponentials formula, and the static model considering gravity loading, actuation loading, and robot constitutive laws is established. Additionally, the effect of tension attenuation caused by routing channel friction is considered in the robot statics, resulting in improved model accuracy. The root-mean-square error between the outputs of the static model and the experimental system is less than 1.63% of the arm length (0.5 m). By employing the proposed static model, a mapping of bending angles between the configuration space and the subsegment space is established. Furthermore, motion control experiments are conducted on our TDQCR system, and the results demonstrate the effectiveness of the static-to-kinematic model.

Keywords: static-to-kinematic modeling scheme, tendon-driven quasi continuum robot, nonconstant subsegment stiffness, tension attenuation effect

PACS: 07.05.Tp, 07.07.Tw, 45.20.D– **DOI:** 10.1088/1674-1056/acfaf8

1. Introduction

Continuum robots, inspired by the natural structures of octopus and elephant trunks, are manipulators composed of multiple flexible segments with slender structure and high flexibility. Different from conventional rigid-link manipulators, continuum robots have the ability to manipulate in complex and constrained environments and are widely used in aero-engine maintenance,[1] nuclear facility inspection,[2] manipulation in confined and cluttered space,[3] human-robot collaboration,[4] and medical applications,[5] etc.

Generally, actuation methods of continuum robots can be mainly divided into hydraulic/pneumatic driven,[6] smart material driven,[7] and tendon-driven.[8] As for tendon-driven continuum robots (TDCRs), the flexible segments are usually equipped with multiple driving tendons. Pulling the tendons results in bending motions of the segments, and the superposition of multisegment bending movements produces the serpentine motion in 3-D space. In 1985, Hemami[9] designed a light weight flexible manipulator composed of multiple flexible subsegments, which is one of the earliest publications on TDCRs. Some continuum manipulators adopt the central backbone structure[10,11] and the backbones can be flexible beams,[12] elastomers,[13,14] springs,[15,16] and bellows;[17,18] while the other designs use multiple flexible backbones with a push-pull actuation, which is a modification of the single backbone structure.[19,20] Nevertheless, robotic arms with flexible skeleton structures tend to have poor load capacity. To address this limitation, Yeshmukhametov *et al.*[21] presented a discrete continuum arm combined with rigid joints and springs, which greatly improved the robot rigidity. Wang *et al.*[22] proposed a novel extra-slender dual-stage continuum robot with various rigid-compliant combined joints to enable different flexibility and stiffness. These rigid-flexible coupling structures offer a good balance between the flexibility and stiffness of the robot and have good development prospects.

The non-constant subsegment stiffness (NSS) structure designed in this paper is a modification of the rigid-flexible coupling structure. Implementing the NSS structure allows one continuum robotic section to be divided into several subsections with variable stiffness, providing desired stiffness for carrying different payloads. Therefore, users can find a trade-off between the load capacity and dexterity depending on the requirements of different tasks.

To achieve the desired performance of continuum robots, fundamental kinematics and statics are required. Note that the soft components of TDCRs make their configuration space representation theoretically require infinite parameters, accurate modeling has always been challenging. On kinematic modeling, most researchers use simplified assumptions to re-

†Corresponding author. E-mail: guoyu@njust.edu.cn

© 2024 Chinese Physical Society and IOP Publishing Ltd

duce the model complexity. The existing methods usually assume that each segment is bent to an arc of constant curvature with no torsion.[23,24] Based on the piecewise-constant-curvature (PCC) assumption, Santina *et al.*[25] proposed an improved state parametrization for soft robots. The parametrization approach can reduce computational burden without incurring in spikes and discontinuous behaviors. Another model simplification approach is to approximate the continuum robot configuration as an n-link manipulator,[26] which is the so-called pseudo rigid body (PRB) modeling method. The main advantage of geometric analysis modeling methods is that robot kinematics can be derived by Denavit–Hartenberg (D-H) parameters, Frenet–Serret frames, and product of exponentials (PoE) formula, etc. However, models based on PCC assumption and PRB method often lead to non-negligible modeling errors.

Considering gravity, inner friction, and robot constitutive laws, static models can deeply reveal the quasi-static characteristics of the manipulator. By applying the Cosserat rod theory, Jones *et al.*[27] introduced a variable curvature model for computing the shape configuration of a continuum robot in 3-D space. Considering inter-subsegment coupling and external disturbance, Chen *et al.*[28] proposed a variable curvature model for quasi continuum robots. Deformation of the manipulator can be determined by using force-torque balance equations. Aiming at ensuring the model accuracy while reducing the computational complexity, discrete Cosserat rod models were derived.[29,30] Additionally, Venkiteswaran *et al.*[31] developed an optimized PRB model, which can estimate the reaction forces and shape of a continuum manipulator. Different from the non-linear Cosserat rod theory, the PRB models use finite elements to represent the robot deformation. However, the iterative solution of static model is time-consuming and difficult to be directly applied to motion control scenarios.

Different from mechanism-based modeling method, data-driven approach is another way to solve the modeling problems of continuum manipulators. In Ref. [32], the inverse kinematic model was obtained by training a multilayer perceptron with a single hidden layer, containing both position and attitude. Giorell *et al.*[33] presented a supervised learning method (feedforward neural network) to solve the inverse static model of non-curvature flexible manipulators, which is faster and more accurate than the iterative inverse algorithm of the Jacobian-based method. In Ref. [34], Elgeneidy *et al.* proposed an empirical model by using regression analysis and artificial neural network. The model is validated by using the new data set generated under untrained operating conditions. However, the data-driven modeling method usually requires a large amount of input and output data. In addition, it is hard to obtain the system model in full space, which limits its further applications.

For a novel TDQCR with the NSS structure designed in this study, the quasi continuum segments composed of stainless steel springs and rigid-flexible coupling subsegments further complicate the robot model. Due to the proposed NSS structure, the change of spring stiffness will result in abrupt changes in subsegment bending properties. In order to achieve comprehensive understanding of the robot motion characteristics, we propose a static-to-kinematic modeling scheme, which can be used in real-time motion control. Contribution details are listed as follows:

1. We design a novel TDQCR with the NSS structure. Different from the existing TDCRs with rigid-flexible coupling units, the novel NSS structure divides one continuum robotic section into several subsections of variable stiffness, facilitating users to find a trade-off between load capacity and dexterity depending on the requirements of different tasks.

2. We derive a static model which can predict deformations of the TDQCR in 3-D space, and the experiments show good consistency between the model and our robot prototype. A novel static-to-kinematic modeling scheme is proposed to reveal the angular mapping characteristics between the configuration space and the subsegment space of the TDQCR, and to validate the feasibility of the model through motion control experiments.

The rest of this paper is organized as follows: Section 2 introduces the kinematics of the TDQCR based on the screw theory. The static model considering gravity loading, tendon tension, multibackbone constitutive laws and tension attenuation effect is then derived by using the Newton–Euler formula in Section 3. In Section 4, experimental results are provided to validate the kinematic and static model. Finally, the conclusions are given in Section 5.

2. Kinematic analysis

2.1. Overview of the TDQCR with the NSS structure

The prototype of a TDQCR section is presented in Fig. 1. Each robotic section contains several 2-DoF rigid-flexible coupling subsegments. Through the push-pull actuation of the tendons, the robotic section can be bent to the corresponding configurations. The subsegments are connected by universal joints, which constitutes the rigid backbone of the continuum arm. The flexible backbone springs are symmetrically arranged in the subsegments and fixed with the upper and lower joint disks.

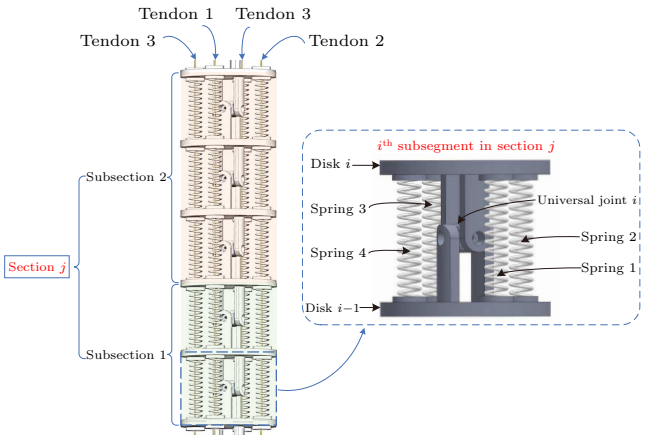


Fig. 1. Schematic diagram of a robotic section of the TDQCR with the NSS structure.

In order to increase load capacity of the manipulator while ensuring the manipulation flexibility, a novel NSS structure is proposed. The wire diameter of backbone springs assembled in the proximal subsegments in each robotic section is larger than that of the distal subsegments. Consequently, one robotic section is divided into several subsections with decreasing stiffness, ensuring the flexibility of the robot motions with fewer actuation units.

2.2. Kinematic modeling based on screw theory

For the TDQCR discussed in this paper, firstly the kinematics of a single subsegment is analyzed. As the displacements of the driven tendons result in the uniform deformations of the subsegment springs, the constant curvature (CC) assumption is then established. By using the screw theory,[35] we develop a concise subsegment-based kinematic model for the continuum manipulator.

As shown in Fig. 2, the configuration of the i^{th} subsegment in the j^{th} section is uniquely determined by the bending angle $\theta_{i,j}$ and the rotation angle $\phi_{i,j}$. The transformation from frame $\{O_{i-1,j}\}$ to frame $\{O_{i,j}\}$ can be expressed as rotation around the screw axis $\hat{s}_{i,j}$, where $\hat{s}_{i,j}$ is orthogonal to the $x'_{i-1,j}O_{i-1,j}z'_{i-1,j}$ plane. Angular velocity $\boldsymbol{\omega}_{i,j} = \left[-\sin(\phi_{i,j})\ \cos(\phi_{i,j})\ 0\right]^{\mathrm{T}}$ is a unit vector determined by rotation angle $\phi_{i,j}$. Taking a point vector $\boldsymbol{q}_{i,j} = \left[l_{i,j}\cot\left(\frac{\theta_{i,j}}{2}\right)\cos(\phi_{i,j})\ l_{i,j}\cot\left(\frac{\theta_{i,j}}{2}\right)\sin(\phi_{i,j})\ 0\right]^{\mathrm{T}}$ on the screw axis $\hat{s}_{i,j}$ (where $l_{i,j}$ is half of the subsegment length), the linear velocity $\boldsymbol{v}_{i,j}$ can be calculated by

$$\boldsymbol{v}_{i,j} = -\boldsymbol{\omega}_{i,j} \times \boldsymbol{q}_{i,j} = \left[0\ 0\ l_{i,j}\cot\left(\frac{\theta_{i,j}}{2}\right)\right]^{\mathrm{T}}. \tag{1}$$

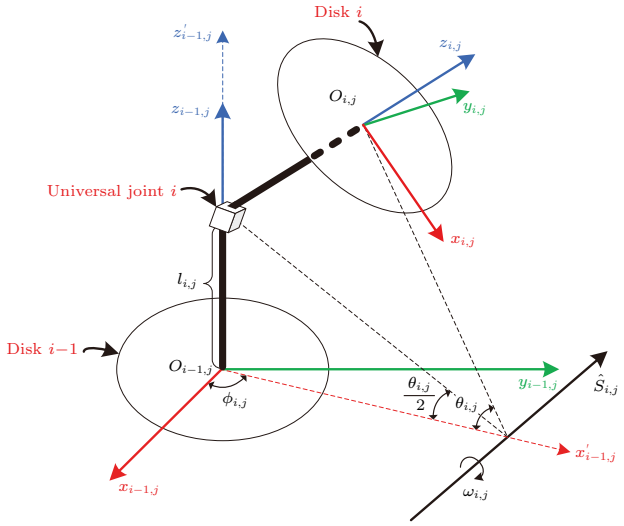


Fig. 2. The sketch chart of a bending subsegment.

We define the spatial twist $\mathcal{S}_{i,j} = (\boldsymbol{\omega}_{i,j}, \boldsymbol{v}_{i,j})$. Unlike the D-H representation, the need of establishing link coordinates is eliminated. By using matrix exponential, the transformation matrix of the adjacent disk frames can be calculated by

$$\boldsymbol{T}_{O_{i,j}}^{O_{i-1,j}} = \mathrm{e}^{[\mathcal{S}_{i,j}]\theta_{i,j}} = \begin{bmatrix} c_{\phi_{i,j}}^2(c_{\theta_{i,j}}-1)+1 & s_{\phi_{i,j}}c_{\phi_{i,j}}(c_{\theta_{i,j}}-1) & c_{\phi_{i,j}}s_{\theta_{i,j}} & l_{i,j}\cot\left(\frac{\theta_{i,j}}{2}\right)c_{\phi_{i,j}}(1-c_{\theta_{i,j}}) \\ s_{\phi_{i,j}}c_{\phi_{i,j}}(c_{\theta_{i,j}}-1) & c_{\phi_{i,j}}^2(c_{\theta_{i,j}}-1)+c_{\theta_{i,j}} & s_{\phi_{i,j}}s_{\theta_{i,j}} & l_{i,j}\cot\left(\frac{\theta_{i,j}}{2}\right)s_{\phi_{i,j}}(1-c_{\theta_{i,j}}) \\ -c_{\phi_{i,j}}s_{\theta_{i,j}} & -s_{\phi_{i,j}}s_{\theta_{i,j}} & c_{\theta_{i,j}} & l_{i,j}\cot\left(\frac{\theta_{i,j}}{2}\right)s_{\theta_{i,j}} \\ 0 & 0 & 0 & 1 \end{bmatrix}, \tag{2}$$

where $c_{\phi_{i,j}} = \cos(\phi_{i,j})$, $s_{\phi_{i,j}} = \sin(\phi_{i,j})$, $c_{\theta_{i,j}} = \cos(\theta_{i,j})$, $s_{\theta_{i,j}} = \sin(\theta_{i,j})$, for the sake of simplification. In this way, the transformation matrix is parameterized by $(\phi_{i,j}, \theta_{i,j}, l_{i,j})$. Evaluating the PoE formula from the base frame $\{O_{0,1}\}$ to the tip frame $\{O_{s_n,n}\}$, we have the subsegment-based forward kinematics of the continuum manipulator as follows:

$$\boldsymbol{T}_{O_{s_n,n}}^{O_{0,1}} = \prod_{j=1}^{n}\left(\prod_{i=1}^{s_j}\mathrm{e}^{[\mathcal{S}_{i,j}]\theta_{i,j}}\right), \tag{3}$$

where n is the number of robot sections, and s_j is the number of subsegments of the j^{th} section.

The kinematic mapping of the TDQCR is illustrated in Fig. 3. Although the forward kinematics from subsegment space to task space is derived by Eq. (3), it is difficult to obtain the subsegment parameter $\theta_{i,j}$. For one robotic section of a TDQCR, its underactuated subsegments move passively with the robotic section. Taking gravity, inner friction, and other non-negligible factors into account, obviously the configuration of the robotic section with the NSS structure is difficultly described with simple geometric relations. Even if the

configuration parameter Θ_j $(j=1,\ldots,n)$ is known, the subsegment bending angles of the j^{th} section remains unknown and the tendon displacement Δl_k in actuation space could not be calculated. To address the bending angle mapping between configuration space and subsegment space, a static model is established under the quasi-static condition.

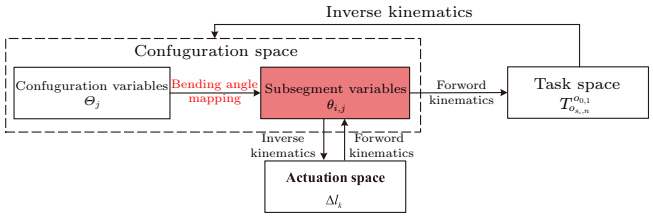


Fig. 3. Kinematic mapping of the TDQCR.

3. Static modeling

In order to improve the accuracy of the static model, tension attenuation effect caused by routing channel friction should be considered when modeling the quasi continuum manipulator. On the basis of considering gravity loading, tendon tensions and constitutive laws generated by the backbone springs, the mechanical modeling of the manipulator is established.

3.1. Forces and moments

3.1.1. Gravity loading by the manipulator

For a comprehensive static model, the gravity effect caused by the joint disks, the universal joints and the backbone springs is non-negligible. As illustrated in Fig. 4, gravity is along the negative direction of z-axis of world frame $\{S\}$. The transformation matrix between world frame $\{S\}$ and robot base frame $\{O_{0,1}\}$ is defined as

$$\boldsymbol{T}^{S}_{O_{0,1}}=\begin{bmatrix}\boldsymbol{R}_S & \boldsymbol{P}_S\\ 0 & 1\end{bmatrix}, \tag{4}$$

where the rotation matrix $\boldsymbol{R}_S$ and translation vector $\boldsymbol{P}_S$ are determined by the assembly configuration of the manipulator. Considering the gravity terms $\boldsymbol{G}^{S}_{\mathrm{d}_{i,j}}$, $\boldsymbol{G}^{S}_{\mathrm{u}_{i,j}}$ and $\boldsymbol{G}^{S}_{s_{i,j}}$ caused by the joint disk, the universal joint and the backbone spring in the i^{th} subsegment of section j, the gravity term $\boldsymbol{G}^{S}$ in frame $\{S\}$ can be calculated as

$$\begin{aligned}\boldsymbol{G}^{S}&=\boldsymbol{G}^{S}_{\mathrm{d}_{i,j}}+\boldsymbol{G}^{S}_{\mathrm{u}_{i,j}}+t_{s_j}\boldsymbol{G}^{S}_{s_{i,j}}\\&=\begin{bmatrix}0 & 0 & -\left(m_{\mathrm{d}_{i,j}}+m_{\mathrm{u}_{i,j}}+t_{s_j}m_{s_{i,j}}\right)\mathrm{g} & 0\end{bmatrix}^{\mathrm{T}},\end{aligned} \tag{5}$$

where $i=1,\ldots,s_j$, $j=1,\ldots,n$; $m_{\mathrm{d}_{i,j}}, m_{\mathrm{u}_{i,j}}, m_{s_{i,j}}$ are the mass of the joint disk, the universal joint and the backbone spring respectively; t_{s_j} is the number of springs in a subsegment in section j. With the help of Eq. (3), the gravity terms can be expressed in the local frame $\{O_{i-1,j}\}$ as follows:

$$\begin{aligned}\boldsymbol{G}^{O_{i-1,j}}&=\boldsymbol{G}^{O_{i-1,j}}_{\mathrm{d}_{i,j}}+\boldsymbol{G}^{O_{i-1,j}}_{\mathrm{u}_{i,j}}+t_{s_j}\boldsymbol{G}^{O_{i-1,j}}_{s_{i,j}}\\&=\left(\boldsymbol{T}^{S}_{O_{0,1}}\boldsymbol{T}^{O_{0,1}}_{O_{i-1,j}}\right)^{-1}\boldsymbol{G}^{S}.\end{aligned} \tag{6}$$

Furthermore, the moments $\boldsymbol{M}^{O_{i-1,j}}_{\mathrm{d}_{i,j}}$, $\boldsymbol{M}^{O_{i-1,j}}_{\mathrm{u}_{i,j}}$ and $\boldsymbol{M}^{O_{i-1,j}}_{s_{i,j}}$ of the gravity terms $\boldsymbol{G}^{S}_{\mathrm{d}_{i,j}}$, $\boldsymbol{G}^{S}_{\mathrm{u}_{i,j}}$ and $\boldsymbol{G}^{S}_{s_{i,j}}$ relative to the origin of frame $\{O_{i-1,j}\}$ can be calculated by

$$\boldsymbol{M}^{O_{i-1,j}}_{\mathrm{d}_{i,j}}=\overrightarrow{O_{i-1,j}d_{i,j}}\times\boldsymbol{G}^{S}_{\mathrm{d}_{i,j}}, \tag{7}$$

$$\boldsymbol{M}^{O_{i-1,j}}_{\mathrm{u}_{i,j}}=\overrightarrow{O_{i-1,j}u_{i,j}}\times\boldsymbol{G}^{S}_{\mathrm{u}_{i,j}}, \tag{8}$$

$$\boldsymbol{M}^{O_{i-1,j}}_{s_{i,j}}=\sum_{k=1}^{t_{s_j}}\overrightarrow{O_{i-1,j}s^{k}_{i,j}}\times\boldsymbol{G}^{S}_{s_{i,j}}, \tag{9}$$

where $d_{i,j}$, $u_{i,j}$, and $s^{k}_{i,j}$ are the center of mass of the joint disk, the universal joint, and the k^{th} backbone spring.

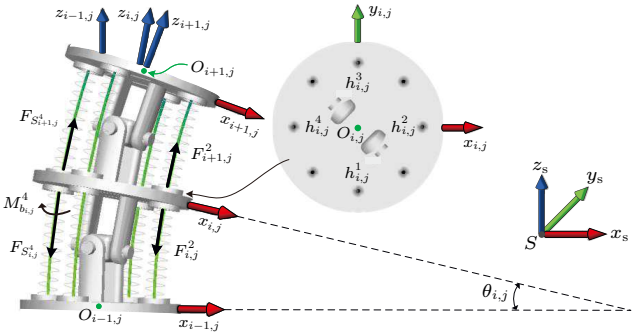


Fig. 4. Force analysis diagram of two adjacent subsegments.

3.1.2. Actuation loading by the driving tendons

Note that each section of the robotic arm is actuated by several tendons. As shown in Fig. 4, the tension $\boldsymbol{F}^{O_{i-1,j}}_{i,j}$ applied to the i^{th} subsegment disk in section j can be calculated by the vector addition of the adjacent tendon tensions $\boldsymbol{F}^{k}_{i,j}$ and $\boldsymbol{F}^{k}_{i+1,j}$, and it can be expressed in the local frame $\{O_{i-1,j}\}$ as

$$\begin{aligned}\boldsymbol{F}^{O_{i-1,j}}_{i,j}&=\sum_{k=1}^{t_{n_j}}\left(\boldsymbol{F}^{k}_{i,j}+\boldsymbol{F}^{k}_{i+1,j}\right)\\&=\sum_{k=1}^{t_{n_j}}\left(\frac{\overrightarrow{h^{k}_{i-1,j}h^{k}_{i,j}}}{\left\|\overrightarrow{h^{k}_{i-1,j}h^{k}_{i,j}}\right\|}f^{k}_{i,j}+\frac{\overrightarrow{h^{k}_{i,j}h^{k}_{i+1,j}}}{\left\|\overrightarrow{h^{k}_{i,j}h^{k}_{i+1,j}}\right\|}f^{k}_{i+1,j}\right),\end{aligned} \tag{10}$$

where $i=1,\ldots,s_j-1$, $j=1,\ldots,n$; $f^{k}_{i,j}$ and $f^{k}_{i+1,j}$ are the values of tensions created by the k^{th} tendon; $h^{k}_{i-1,j}$, $h^{k}_{i,j}$ and $h^{k}_{i+1,j}$ are the positions of the routing channels expressed in the local frame $\{O_{i-1,j}\}$; and t_{n_j} is the total number of tendons acting on the j^{th} section.

The sum of moments relative to the origin of frame $\{O_{i-1,j}\}$ can be calculated by

$$\begin{aligned}\boldsymbol{M}^{O_{i-1,j}}_{i,j}=\sum_{k=1}^{t_{n_j}}&(\overrightarrow{O_{i-1,j}h^{k}_{i,j}}\times\boldsymbol{F}^{k}_{i,j}\\&+\overrightarrow{O_{i-1,j}h^{k}_{i+1,j}}\times\boldsymbol{F}^{k}_{i+1,j}).\end{aligned} \tag{11}$$

Specially, the total tension applied to the last subsegment disk of each section (i.e., $i = s_j$, $j = 1, \ldots, n$) is calculated by

$$\boldsymbol{F}_{s_j,j}^{O_{s_j-1,j}} = \begin{cases} \sum_{k=1}^{t_{n_j}} \boldsymbol{F}_{s_j,j}^k + \sum_{k=1}^{t_{n_{j+1}}} \boldsymbol{F}_{1,j+1}^k \\ \sum_{k=1}^{t_{n_j}} \boldsymbol{F}_{s_j,j}^k \end{cases} = \begin{cases} \sum_{k=1}^{t_{n_j}} \dfrac{\overrightarrow{h_{s_j-1,j}^k h_{s_j,j}^k}}{\left\|\overrightarrow{h_{s_j-1,j}^k h_{s_j,j}^k}\right\|} f_{s_j,j}^k + \sum_{k=1}^{t_{n_{j+1}}} \dfrac{\overrightarrow{h_{s_j,j}^k h_{1,j+1}^k}}{\left\|\overrightarrow{h_{s_j,j}^k h_{1,j+1}^k}\right\|} f_{1,j+1}^k, \\ \qquad\qquad (1 \le j < n), \\ \sum_{k=1}^{t_{n_j}} \dfrac{\overrightarrow{h_{s_j-1,j}^k h_{s_j,j}^k}}{\left\|\overrightarrow{h_{s_j-1,j}^k h_{s_j,j}^k}\right\|} f_{s_j,j}^k, \quad (j = n). \end{cases} \tag{12}$$

The total moment provided by the tensions is expressed as

$$\boldsymbol{M}_{s_j,j}^{O_{s_j-1,j}} = \begin{cases} \sum_{k=1}^{t_{n_j}} \boldsymbol{M}_{s_j,j}^k + \sum_{k=1}^{t_{n_{j+1}}} \boldsymbol{M}_{1,j+1}^k \\ \sum_{k=1}^{t_{n_j}} \boldsymbol{M}_{s_j,j}^k \end{cases} = \begin{cases} \sum_{k=1}^{t_{n_j}} \overrightarrow{O_{s_j-1,j} h_{s_j,j}^k} \times \boldsymbol{F}_{s_j,j}^k + \sum_{k=1}^{t_{n_{j+1}}} \overrightarrow{O_{s_j,j} h_{1,j+1}^k} \times \boldsymbol{F}_{1,j+1}^k, \\ \qquad\qquad (1 \le j < n), \\ \sum_{k=1}^{t_{n_j}} \overrightarrow{O_{s_j-1,j} h_{s_j,j}^k} \times \boldsymbol{F}_{s_j,j}^k, \quad (j = n). \end{cases} \tag{13}$$

3.2. Tension attenuation effect

Most static models for tendon driving systems assume that the tension is the same everywhere in a single tendon. However, this is inconsistent with the physical system. Friction between the driving tendon and the routing channel is affected by many factors, such as material properties, geometric dimensions and lubrication effect. Figure 5 shows the tension attenuation effect of routing channel $h_{i,j}^k$ in the i^{th} subsegment disk of section j.

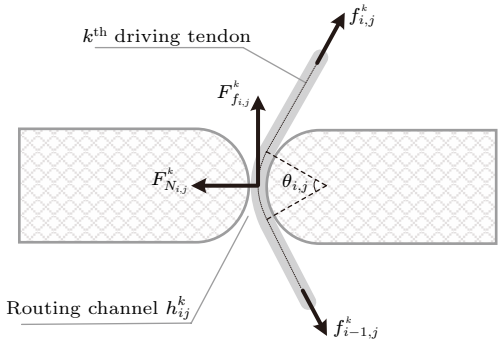


Fig. 5. The sketch chart of tension attenuation effect.

As the continuum robot often works at a slow speed, it is assumed in this study that the sliding friction is approximately equal to the static friction. When the bending angle $\theta_{i,j}$ varies, the positive pressure $F_{N_{i,j}}^k$ that the tendon applies on the routing channel becomes different, leading to a change in the deformation of the tendon in contact with the routing channel. According to the force balance equation, we have

$$f_{i,j}^k \cos\left(\frac{\theta_{i,j}}{2}\right) - f_{i,j-1}^k \cos\left(\frac{\theta_{i,j}}{2}\right) = \mu F_{N_{i,j}}^k, \tag{14}$$

$$f_{i,j}^k \sin\left(\frac{\theta_{i,j}}{2}\right) + f_{i,j-1}^k \sin\left(\frac{\theta_{i,j}}{2}\right) = F_{N_{i,j}}^k, \tag{15}$$

where μ is the static friction coefficient. Substituting Eq. (15) into Eq. (14), we can obtain the attenuated tendon tension through the routing channel:

$$f_{i,j}^k = \frac{\cos\left(\frac{\theta_{i,j}}{2}\right) - \mu \sin\left(\frac{\theta_{i,j}}{2}\right)}{\cos\left(\frac{\theta_{i,j}}{2}\right) + \mu \sin\left(\frac{\theta_{i,j}}{2}\right)} f_{i,j-1}^k = \alpha_{i,j} f_{i,j-1}^k. \tag{16}$$

Dividing the bending angle $\theta_{i,j}$ into infinitesimal angle micro elements, the tension attenuation coefficient $\alpha_{i,j}$ can be calculated by

$$\alpha_{i,j} = \lim_{N \to +\infty} \left(\frac{\cos\left(\frac{\theta_{i,j}}{2N}\right) - \mu \sin\left(\frac{\theta_{i,j}}{2N}\right)}{\cos\left(\frac{\theta_{i,j}}{2N}\right) + \mu \sin\left(\frac{\theta_{i,j}}{2N}\right)} \right)^N = \mathrm{e}^{-\mu\theta_{i,j}}. \tag{17}$$

3.3. Constitutive and equilibrium equations

When the robotic arm bends, the backbone springs in the subsegments are stretched or compressed, creating forces and bending moments on the attached disks. The force $f_{s_{i,j}}^k$ on the i^{th} disk of section j in the k^{th} routing channel can be calculated by adding forces $f_{s_{i,j}^k}$ and $f_{s_{i+1,j}^k}$ from the adjacent spring deformations:

$$f_{s_{i,j}}^k = f_{s_{i,j}^k} + f_{s_{i+1,j}^k} = k_{i,j} \Delta l_{i,j}^k + k_{i+1,j} \Delta l_{i+1,j}^k, \tag{18}$$

where $i = 1, \ldots, s_j - 1$, $j = 1, \ldots, n$; $k_{i,j}$ and $k_{i+1,j}$ are the stiffness coefficients of the springs; $\Delta l_{i,j}^k$ and $\Delta l_{i+1,j}^k$ are the spring deformations.

Special cases need to be considered. The force on the last subsegment disk of each section (i.e., $i = s_j$, $j = 1, \ldots, n$) is calculated by

$$f_{s_{s_j,j}}^k = \begin{cases} f_{s_{s_j,j}^k} + f_{s_{1,j+1}^k} \\ f_{s_{s_j,j}^k} \end{cases} = \begin{cases} k_{s_j,j} \Delta l_{s_j,j}^k + k_{1,j+1} \Delta l_{1,j+1}^k, & (1 \le j < n), \\ k_{s_j,j} \Delta l_{s_j,j}^k, & (j = n). \end{cases} \tag{19}$$

Obviously, the direction of $f_{s_{i,j}}^k$ is parallel to the $z_{i,j}$ axis and $f_{s_{i,j}}^k$ spans to vector $\boldsymbol{F}_{s_{i,j}}^k = \begin{bmatrix} 0 & 0 & f_{s_{i,j}}^k & 0 \end{bmatrix}^{\mathrm{T}}$. The transformation matrix between frame $\{O_{i,j}\}$ and routing channel $h_{i,j}^k$ is defined as

$$\boldsymbol{T}_{h_{i,j}^k}^{O_{i,j}} = \begin{bmatrix} \boldsymbol{I}_3 & \overrightarrow{O_{i,j} h_{i,j}^k} \\ 0 & 1 \end{bmatrix}, \tag{20}$$

where $\boldsymbol{I}_3$ denotes the third order identity matrix. $\overrightarrow{O_{i,j}h^k_{i,j}}$ is the translation vector between the origin of frame $\{O_{i-1,j}\}$ and routing channel $h^k_{i,j}$. Using Eqs. (2) and (20), we have

$$\boldsymbol{F}^{O_{i-1,j}}_{s_{i,j}} = \sum_{k=1}^{t_{s_j}} \left(\boldsymbol{T}^{O_{i-1,j}}_{O_{i,j}} \boldsymbol{T}^{O_{i,j}}_{h^k_{i,j}} \boldsymbol{F}^k_{s_{i,j}}\right). \tag{21}$$

The lateral bending moment of a spring is a function of angular deflection $\theta_{i,j}$, material properties, elastic modules E and Poisson's ratio v,[36] which can be calculated as

$$M_{b_{i,j}} = \frac{E\left(d_{s_{i,j}}\right)^4}{32N_{s_{i,j}}(2+v)D_{i,j}}\theta_{i,j}, \tag{22}$$

where $d_{s_{i,j}}$ is the wire diameter of the spring in the i^{th} subsegment in section j, $D_{i,j}$ is the coil diameter, and $N_{s_{i,j}}$ is the number of active coils. The homogeneous vector of lateral bending moment $\boldsymbol{M}_{b_{i,j}} = \begin{bmatrix}0 & t_{s_j}M_{b_{i,j}} & 0 & 0\end{bmatrix}^{\mathrm{T}}$. As the springs in a single subsegment share the same bending angle $\theta_{i,j}$, the moment in frame $\{O_{i-1,j}\}$ is

$$\boldsymbol{M}^{O_{i-1,j}}_{b_{i,j}} = \boldsymbol{T}^{O_{i-1,j}}_{O_{i,j}} \boldsymbol{M}_{b_{i,j}}. \tag{23}$$

Combining with Eqs. (4)–(23), we can analyze the statics of the TDQCR comprehensively. Equilibrium equations are derived based on the Newton–Euler formula as follows:

$$\boldsymbol{F}^{O_{i-1,j}} = \boldsymbol{G}^{O_{i-1,j}} + \boldsymbol{F}^{O_{i-1,j}}_{i,j} + \boldsymbol{F}^{O_{i-1,j}}_{s_{i,j}} + \boldsymbol{T}^{O_{i-1,j}}_{O_{i,j}} \boldsymbol{F}^{O_{i,j}}, \tag{24}$$

$$\begin{aligned}\boldsymbol{M}^{O_{i-1,j}} = {} & \boldsymbol{M}^{O_{i-1,j}}_{\mathrm{d}_{i,j}} + \boldsymbol{M}^{O_{i-1,j}}_{\mathrm{u}_{i,j}} + \boldsymbol{M}^{O_{i-1,j}}_{s_{i,j}} + \boldsymbol{M}^{O_{i-1,j}}_{i,j} + \boldsymbol{M}^{O_{i-1,j}}_{b_{i,j}} \\ & + \boldsymbol{T}^{O_{i-1,j}}_{O_{i,j}} \boldsymbol{M}^{O_{i,j}} + \overrightarrow{O_{i-1,j}O_{i,j}} \times \boldsymbol{F}^{O_{i,j}}.\end{aligned} \tag{25}$$

As for the tip frame (i.e., $i = s_n$, $j = n$), the recursive terms $\boldsymbol{F}^{O_{i,j}}$ and $\boldsymbol{M}^{O_{i,j}}$ in Eqs. (24) and (25) are equal to zero. The problem is transformed into solving the subsegment parameters $\theta_{i,j}$ and $\phi_{i,j}$ according to the actuation forces. With the help of the function *fsolve* implemented in software Octave, the nonlinear equations are solved by recursive calculations.

4. Experiments and discussion

4.1. Experimental setup

To verify the feasibility and accuracy of the proposed static model, experimental validation was conducted for the TDQCR designed in this paper [robotic prototype is shown in Fig. 6(a)]. Diameter of the subsegment disk is 0.06 m and the diameter-to-length ratio is 0.12. The static friction coefficient μ is set to 0.2. Detailed parameters of the TDQCR are listed in Table 1. In Fig. 6(a), specific tendon tensions were generated by attaching standard weights to the end of the driving tendons. The pose of each joint disk was measured by the AprilTags visual fiducial system.[37] The tags from tag family Tag36h11 were detected by a 1920×1080 pixel camera (Intel® RealSense™ Depth Camera D435i). The camera was placed at the lab table, facing the robot arm along the negative direction of y-axis of world frame $\{S\}$. Before experiments, the camera was calibrated and precision of the vision measuring system is ± 0.2 mm. Figure 6(b) illustrates the simplified static simulation visualization model of the TDQCR constructed in Octave.

Table 1. Parameters of the proposed TDQCR.

Name	Value
Number of sections	$n = 2$
Subsegment dimensions	$s_1 = 5, s_2 = 5$
Tendon dimensions	$t_{n_1} = 8, t_{n_2} = 4$
Spring dimensions	$t_{s_1} = 4, t_{s_2} = 4$
Mass of the body disk	$m_{d_{i,j}} = 24.0$ g
Mass of the tip disk	$m_{d_{s_2,n}} = 21.1$ g
Mass of the universal joint	$m_{u_{i,j}} = 2.8$ g
Bending capacity of each subsegment	$-45^\circ \le \theta_{i,j} \le 45^\circ$
Half of the subsegment length	$l_{i,j} = 25$ mm

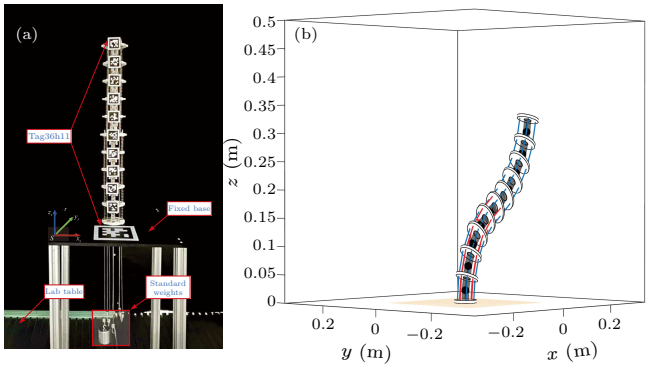


Fig. 6. Experimental setup: (a) the testbed with AprilTags visual fiducial system, (b) the static simulation model of the TDQCR.

To specify the novel NSS structure utilized in the robot design, the parameters of backbone springs are listed in Table 2. Note that the springs are made of stainless steel and Young's modulus $E \approx 190$ GPa, Poisson's ratio $v \approx 0.35$.

Table 2. Parameters of the backbone springs.

Name	Subsegment index		
	1–2	3–8	9–10
Wire diameter	1.4 mm	1.2 mm	1.0 mm
Coil diameter	9 mm	9 mm	9 mm
Number of coils	13	14	15
Mass of spring	2.6 g	2.0 g	1.6 g

4.2. Statics validation

4.2.1. Single tendon actuation

Here two experiment sets were performed under single tendon actuation. Due to the symmetry of the robotic structure, the effect of driving any tendon of a robotic section is essentially the same. Tendon t_{12} in the first section and tendon t_{22} in the second section were chosen, and detailed results are presented.

The snapshots of the manipulator under different pulling forces are overlapped in Fig. 7. The weight applied to tendon t_{12} was increased from 100 g to 1700 g with intervals of 200 g, and a total of 9 groups of data were obtained. The first robotic section was bent to the positive direction of x-axis while the second section remained almost straight. The manipulator was continuously bent with the increase of tendon tension. Meanwhile, due to the influence of gravity and the nonlinearity of flexible components, the bending angle of the first section did not increase uniformly.

Figure 8 shows the comparison of experimental measurement positions and model-based positions under the actuation of tendon t_{12}. It is clear that the model results are highly consistent with the prototype. The proposed static model can predict the manipulator deformation with high accuracy. The calculated root-mean-square error (RMSE) is 3.7×10^{-3} m and the maximum error is 5.3×10^{-3} m, which only account for 0.77% and 1.11% of the entire arm length (i.e., 0.50 m).

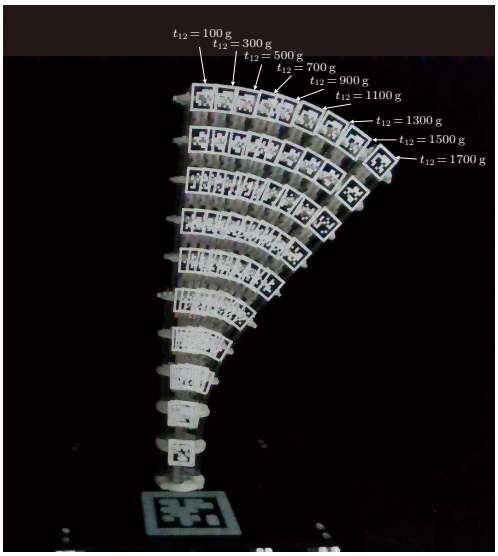


Fig. 7. Single tendon actuation by tendon t_{12}.

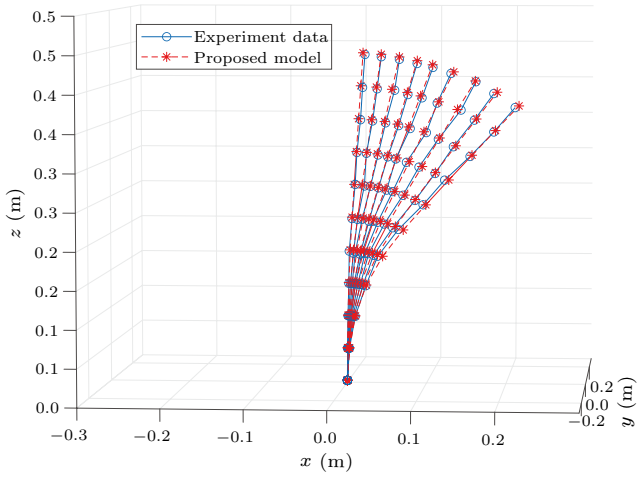


Fig. 8. Comparison between the experimental results and the model results (TDQCR deformations caused by tendon tension t_{12} varied from 100 g to 1700 g with intervals of 200 g).

Figures 7 and 8 represent the in-plane results. Figure 9 and 10 show the results of the out-of-plane cases. The weight applied to tendon t_{22} was increased from 200 g to 1600 g with intervals of 200 g, and totally 8 groups of data were obtained. The tendon tension t_{22} was increased gradually, and the second section was bent. The first section was passively bent due to the coupling effect between the sections (see Fig. 9). As shown in Fig. 10, the static model can still well predict the deformation of the robotics arm. The obtained RMSE and maximum error are 7.8×10^{-3} m and 1.13×10^{-2} m, respectively, accounting for 1.63% and 2.35% of the entire length of the manipulator.

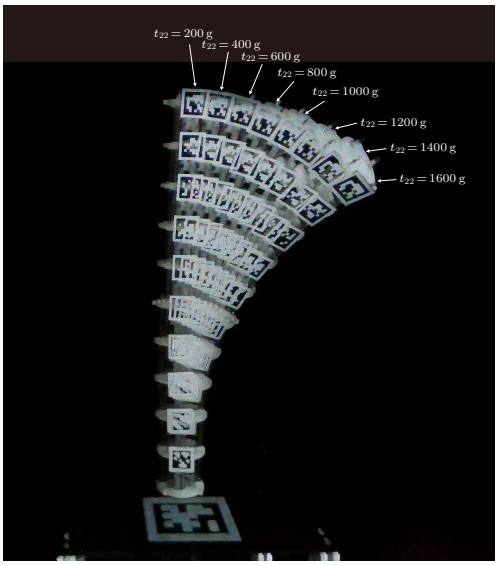


Fig. 9. Single tendon actuation by tendon t_{22}.

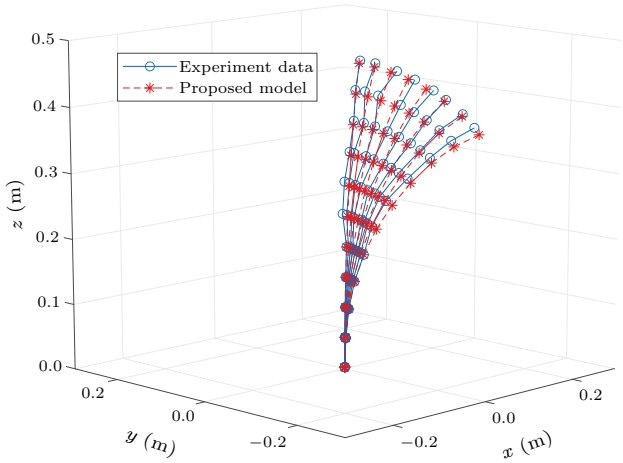


Fig. 10. Comparison between the experimental results and the model results (TDQCR deformations caused by tendon tension t_{22} varied from 200 g to 1600 g with intervals of 200 g).

4.2.2. Symmetrical tendon actuation

To further verify the proposed static model, experiments of symmetric tendon actuation were carried out. The overlays of the experiment snapshots are similar to those of the previous

subsegment and are not repeated below. As shown in Fig. 11, one tendon tension was fixed, and the other tendon tension was increased gradually. The outputs of the static model and experimental system reflect good symmetry properties of the manipulator. The RMSE and maximum error are 4.4×10^{-3} m and 6.7×10^{-3} m, respectively, accounting for 0.92% and 1.39% of the entire length of the manipulator, which are almost consistent with the cases of single tendon actuation.

The out-of-plane experiments by symmetrical tendon actuation are shown in Fig. 12. Similar to Fig. 10, the errors of out-of-plane experiments are larger than those of the in-plane cases. The obtained RMSE and maximum error are 5.9×10^{-3} m and 1.0×10^{-2} m, respectively, accounting for 1.23% and 2.08% of the entire length of the manipulator. The accuracy of the proposed static model is still maintained at a high level.

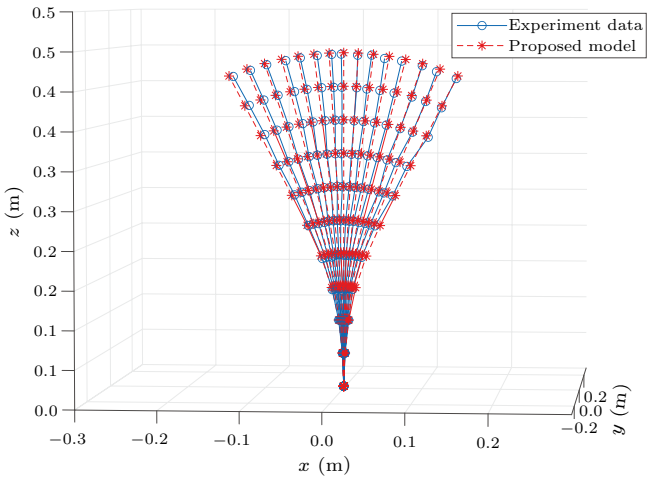


Fig. 11. Symmetrical tendon actuation by tendons t_{12} and t_{14}: one tendon tension was fixed at 300 g and the other tendon tension varied from 300 g to 1700 g with intervals of 200 g.

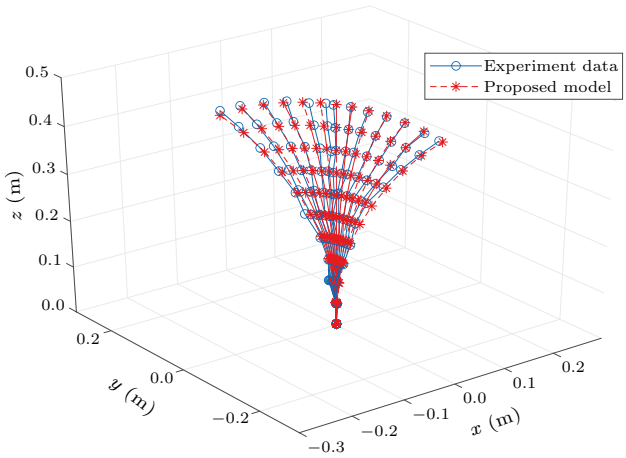


Fig. 12. Symmetrical tendon actuation by tendons t_{22} and t_{24}: one tendon tension was fixed at 400 g and the other tendon tension varied from 400 g to 1600 g with intervals of 200 g.

4.3. NSS structure analysis

Implementing the NSS structure allows one continuum robotic section to be divided into multiple subsections with variable stiffness, providing selective stiffness for carrying different payloads. We conducted a simulation to analyze its load ability. We set high and medium spring stiffness (same parameters as high stiffness spring and medium stiffness spring of the NSS structure) and constructed the TDQCR for two stiffness configurations. As shown in Fig. 13, the tension of tendon t_{22} was gradually increased from 0 g to 2000 g, with intervals of 10 g. Height t_Z of the tip of the medium stiffness TDQCR is the first to drop below 0 m, and the corresponding tendon tension is 670 g. Similarly, the corresponding tendon tensions for the NSS and high stiffness TDQCR are 1390 g and 1600 g, respectively. Furthermore, we applied a load of 100 g at the robot tip of different stiffness configurations to compare the load effect (see Fig. 14). When the tendon tension t_{22} gradually increased from 0 g to 500 g, the height deflection of the TDQCR with medium stiffness configuration is the largest one. The maximum deviation exceeds 0.17 m (34% of the arm length), which is far greater than the other two stiffness configurations. The load capacity of the NSS structure is close to that of the high stiffness configuration.

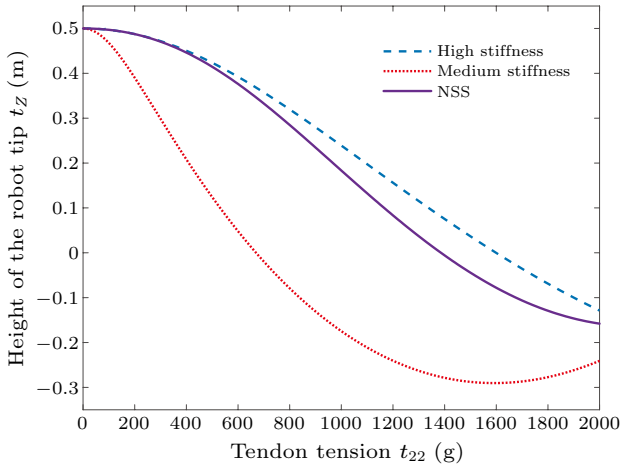


Fig. 13. Height t_Z of the robot tip under the tensioning of tendon t_{22}.

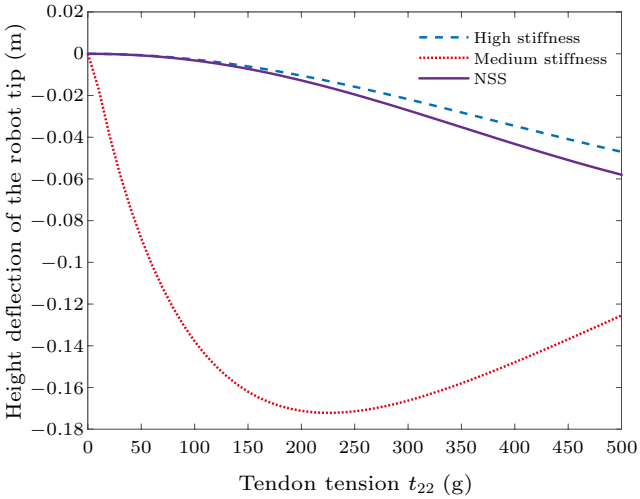


Fig. 14. Height deflection of the robot tip caused by 100 g load under the same tendon tension.

In summary, the flexibility and load capacity of a TDCR are always contradictory. High stiffness configurations can effectively increase the load capacity but place an additional burden on the actuation unit and sacrifice the flexibility of the manipulator. In contrast, low stiffness configurations are generally more flexible, but the load capacity are greatly decreased. Our new NSS structure is a trade-off between load capacity and dexterity, allowing users to set the number of sections and stiffness configuration of the robot to meet different task requirements.

4.4. Static-to-kinematic modeling and verification

The results of the statics validation are summarized in Table 3. The static model can well reflect the quasi-static characteristics of the manipulator and provide a theoretical basis for the optimal design and kinematic motion control.

Table 3. Errors between experimental results and the proposed static model.

Types of actuation	Absolute value/Relative value	
	RMSE	Maximum error
Single tendon (t_{12})	3.7 mm/0.77%	5.3 mm/1.11%
Single tendon (t_{22})	7.8 mm/1.63%	1.1 mm/2.35%
Symmetrical tendons (t_{12} & t_{14})	4.4 mm/0.92%	6.7 mm/1.39%
Symmetrical tendons (t_{22} & t_{24})	5.9 mm/1.23%	12 mm/2.08%

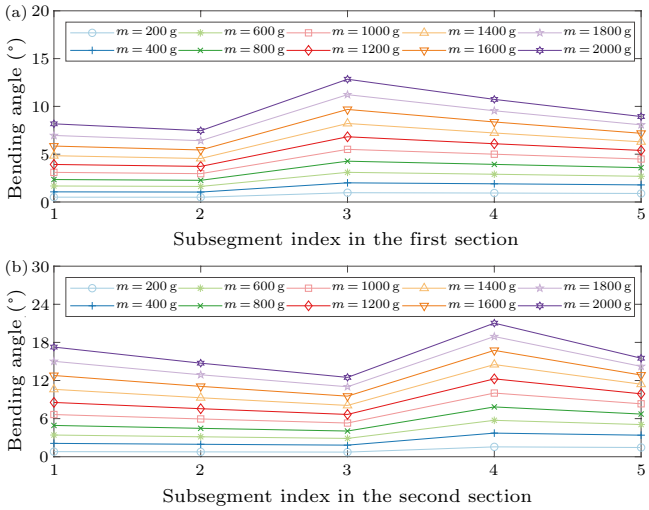


Fig. 15. Bending angle of the subsegments: (a) deflection of the first section under the tensioning of tendon t_{12}, (b) deflection of the second section under the tensioning of tendon t_{22}.

In order to find the bending angle mapping between the configuration space and the subsegment space, two bending angle datasets were produced in quasi-static workspace based on numerical calculations. As shown in Figs. 15(a) and 16(a), the tendon tension t_{12} was gradually increased from 50 g to 2000 g with intervals of 10 g, constituting one dataset. Under the same tendon tension, the bending angle of subsegments from 1 to 2 in the first robotic section decreases, and the bending angle of subsegments from 3 to 5 decreases [see Fig. 15(a)]. Moreover, the bending angle increases sharply at the third subsegment bending angle, and the first section is then divided into two subsections, which is consistent with the proposed NSS structure. The proportion of the bending angle of each subsegment is approximately linear to the total bending angle [Fig. 16(a)]. Similarly, the other dataset was obtained by increasing the tendon tension t_{22} from 50 g to 2000 g with intervals of 10 g. Figure 15(b) shows that under the same tendon tension, the bending angle of subsegments from 1 to 3 in the second robotic section decreases, and the bending angle of subsegments from 4 to 5 decreases. A steep increase is shown at the fourth subsegment bending angle. The proportion of the bending angle of each subsegment is also approximately linear to the total bending angle of the second section [Fig. 16(b)].

The above results reveal the abrupt change of subsegment bending angle caused by the NSS structure. Using our static simulation model, one can obtain sufficient static workspace which includes the mapping of manipulator configuration and subsegment bending angles. The static-to-kinematic model was proposed by combining the static workspace with the kinematic model. On the basis, the bending angle mapping between the configuration space and the subsegment space was found, and the actuation variables Δl_k were calculated by configuration variables Θ_j and subsegment variables $\theta_{i,j}$ (see Fig. 3).

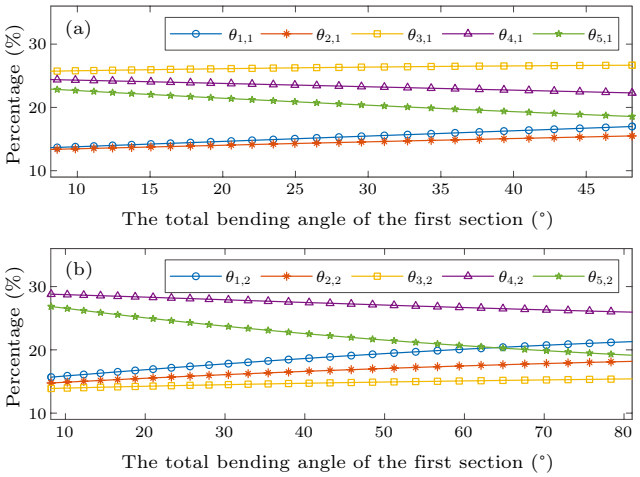


Fig. 16. The proportion of bending angle of each subsegment: (a) tendon tension t_{12} gradually increased from 50 g to 2000 g with intervals of 10 g, (b) tendon tension t_{22} gradually increased from 50 g to 2000 g with intervals of 10 g.

To verify the static-to-kinematic model, motion control experiments were conducted on our TDQCR system (see Fig. 17(a)). The control of the robotic arm is facilitated by an Arduino Uno R3 microcontroller board, which receives commands from the PC and governs the arm's motion. The robotic arm consists of two sections, with each section comprising five 2-DOF subsegments. The length of the driving tendons is determined according to the desired manipulator configuration,

and a lead screw is employed to convert rotational motion into linear motion, enabling a push-pull actuation mechanism [see Fig. 17(b)]. The manipulator is actuated to specific configurations by controlling the length of the tendons. Real-time tendon tension data is continuously collected using force sensors, enabling analysis of the manipulator's movement process. Once the manipulator reaches the desired configuration and maintains stability, the collected tendon tension is employed in the proposed static model to calculate the manipulator's bending. This calculated configuration is then compared with the output of our robotic prototype system.

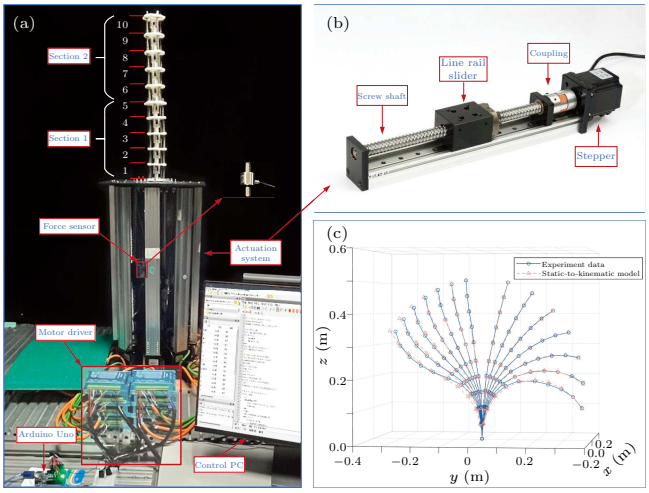


Fig. 17. Robot system and motion control results: (a) tendon-driven quasi continuum robot system, (b) actuation system, and (c) motion control data and static-to-kinematic model results.

We controlled the two-section TDQCR for C-shaped and S-shaped bending motions. The segmental bending angle was increased from 10° to 70°. By utilizing the proposed static-to-kinematic model, it becomes possible to calculate the subsegmental bending angles corresponding to various robot arm shapes, thereby achieving a more precise calculation of the driving tendon length. It can be seen from Fig. 17(c) that the results of our static-to-kinematic model are in good agreement with the actual robot configurations. Under the C-shaped configurations, the outputs of our model are almost consistent with the outputs of the actual robot system. However, in S-shaped configurations, as the bending angle increases, the mismatching phenomenon becomes relatively significant. This discrepancy can be attributed to the amplified influence of coupling among robotic sections in complex configurations. For different stiffness designs of the manipulator, one need only change the mechanical parameters of the robotic arm in the static model to obtain the subsegment bending characteristics. Therefore, this static-to-kinematic modeling scheme is of good generality for the modeling of continuum manipulators.

5. Conclusions

This paper presents a TDQCR manipulator with the innovative NSS structure, which can provide desired stiffness for carrying different payloads. To analyze the kinematics and statics of the TDQCR, the subsegment-based kinematics is derived by using screw theory. Considering gravity loading, tendon tension, multibackbone constitutive laws, and tension attenuation effect, the static model is established and validated by experiments. The results indicate that the theoretical model is highly consistent with the prototype.

To solve the bending angle mapping problem between the configuration space and the subsegment space, the static-to-kinematic model is proposed. Motion control experiments show the superiority of our static-to-kinematic model. Moreover, this modeling scheme can be possibly applied to various types of continuum manipulators, demonstrating a solid foundation for the robot motion control. Future work will focus on the dynamic modeling and the motion planning of the TDQCR.

Acknowledgements

Project supported by the National Natural Science Foundation of China (Grant No. 61973167) and the Jiangsu Funding Program for Excellent Postdoctoral Talent.

References

[1] Ba W M, Dong X, Mohammad A, Wang M F, Axinte D and Norton A 2021 *IEEE/ASME Trans. Mechatronics* **26** 3010
[2] Mohammad A, Russo M, Fang Y H, Dong X, Axinte D and Kell J 2021 *IEEE Robot. Autom. Lett.* **6** 7493
[3] Wang M Y, Du L, Yuan J J, Ma S G and Bao S 2021 *IEEE International Conference on Robotics and Biomimetics (ROBIO)*, December 27-31, Sanya, China, p. 74
[4] Müller D, Veil C, Seidel M and Sawodny O 2020 *Mechatronics* **70** 102418
[5] Dupont PE, Simaan N, Choset H and Rucker C 2022 *Proc. IEEE Inst. Electr. Electron. Eng.* **110** 847
[6] Peng Y, Liu Y G, Yang Y, Liu N, Sun Y, Liu Y Y, Pu H Y, Xie S R and Luo J 2019 *Mechatronics* **60** 56
[7] He B, Zhang C H and Ding A 2017 *Chin. Phys. B* **26** 126102
[8] Rus D and Tolley M T 2015 *Nature* **521** 467
[9] Hemami A 1985 *Robotics* **1** 27
[10] Wooten M B and Walker I D 2022 *IEEE Robot. Autom. Lett.* **7** 10136
[11] Yuan H and Li Z 2018 *Robot. Comput.-Integr. Manuf.* **49** 240
[12] Mo H J, Wei R F, Ouyang B, Xing L X, Shan Y H, Liu Y H and Sun D 2021 *IEEE Robot. Autom. Lett.* **6** 1074
[13] Wang Q, Yong Y Q and Bai Z M 2022 *Chin. Phys. B* **31** 128801
[14] Uppalapati N K and Krishnan G 2021 *J. Mech. Robot.* **13** 011010
[15] Qin L, Liang X Q, Huang H, Chui C K, Yeow R C and Zhu J 2019 *Soft Robot.* **6** 455
[16] Tamadon I, Huan Y, de Groot A G, Menciassi A and Sinibaldi E 2020 *Int. J. Med. Robot. Comput. Assist. Surg* **16** e2072
[17] Yukisawa T, Ishii Y, Nishikawa S, Niiyama R and Kuniyoshi Y 2017 *IEEE International Conference on Robotics and Biomimetics (ROBIO)* December 5–8, Macau, Macao, p. 2303
[18] Sui D B, Zhao S K, Wang T S, Liu Y B, Zhu Y H and Zhao J 2022 *J. Bionic Eng.*
[19] Xu K and Simaan N 2010 *J. Mech. Robot.* **2** 011006

[20] Zhao B, Zhang W H, Zhang Z Y, Zhu X Y and Xu K 2018 *IEEE/RSJ International Conference on Intelligent Robots and Systems (IROS)* October 01–05, Madrid, Spain, p. 7492

[21] Yeshmukhametov A, Koganezawa K and Yamamoto Y 2019 *Robotics* **8** 51

[22] Wang M F, Dong X, Ba W M, Mohammad A, Axinte D and Norton A 2021 *Robot. Comput.-Integr. Manuf.* **67** 102054

[23] Li M H, Kang R J, Geng S N and Guglielmino E 2018 *Trans. Inst. Meas. Control.* **40** 3263

[24] Barrientos-Diez J, Dong X, Axinte D and Kell J 2021 *Robot. Comput.-Integr. Manuf.* **67** 102019

[25] Della Santina C, Bicchi A and Rus D 2020 *IEEE Robot. Autom. Lett.* **5** 1001

[26] Greigarn T and Çavuşoğlu M C 2014 *IEEE/RSJ International Conference on Intelligent Robots and Systems* September 14–88, Chicago, IL, USA, p. 3476

[27] Jones B A, Gray R L and Turlapati K 2009 *IEEE/RSJ International Conference on Intelligent Robots and Systems* October 10–15, St. Louis, MO, USA, p. 2659

[28] Chen Y Y, Wu B B, Jin J B and Xu K 2021 *IEEE Robot. Autom. Lett.* **6** 1590

[29] Renda F, Boyer F, Dias J and Seneviratne L 2018 *IEEE Trans. Robot.* **34** 1518

[30] Grazioso S, Di Gironimo G and Siciliano B 2019 *Soft Robot.* **6** 790

[31] Venkiteswaran V K, Sikorski J and Misra S 2019 *Mech. Mach. Theory* **139** 34

[32] Thuruthel T G, Falotico E, Manti M, Pratesi A, Cianchetti M and Laschi C 2017 *Soft Robot.* **4** 285

[33] Giorelli M, Renda F, Calisti M, Arienti A, Ferri G and Laschi C 2015 *IEEE Trans. Robot.* **31** 823

[34] Elgeneidy K, Lohse N and Jackson M 2018 *Mechatronics* **50** 234

[35] Lynch K M and Park F C 2017 *Modern Robotics* (Cambridge: Cambridge University Press) p. 118

[36] Keller S G and Gordon A P 2011 *Strain Anal. Eng. Des* **46** 405

[37] Krogius M, Haggenmiller A and Olson E 2019 *IEEE/RSJ International Conference on Intelligent Robots and Systems (IROS)* November 03–08, Macau, China, p. 1898